ACS APPLIED ENERGY MATERIALS

www.acsaem.org

Article

Self-Heating of Planar Perovskite Solar Cells Depending on Active Material Properties

Aleksi Kamppinen,* Heikki Palonen, and Kati Miettunen

Cite This: https://doi.org/10.1021/acsaem.4c00077

Read Online

ACCESS | Metrics & More | Article Recommendations | Supporting Information

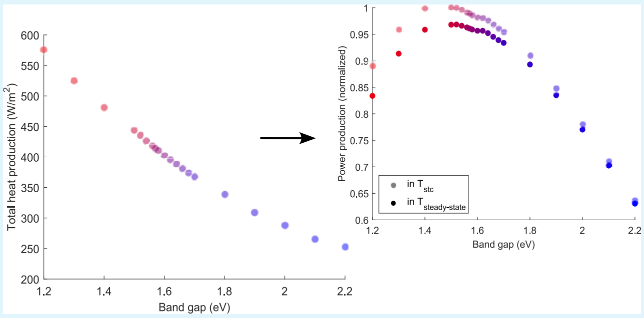

ABSTRACT: The effect of perovskite material properties on the power conversion to electricity and, especially, to heat and the operation temperature of perovskite solar cells (PSCs) was simulated. The operation temperature is topical because the technology is progressing toward commercialization: first, because cells are subject to varying outdoor conditions, and second, because commercial use benefits from accurate power production prediction, in which the cell temperature is an influential factor. This article products insights into how perovskite absorber properties, including the band gap (E_g), diffusion length, and layer thickness, affect the heat production and temperature coefficient of planar PSCs based on optoelectronic simulations. The change in heat production with an increasing band gap was observed to be quasi-linear: self-heating decreased by approximately -0.38 W/(m^2 meV) until E_g = 1.7 eV, after which the slope slightly relaxed. Over the studied band gap range of 1.2−2.2 eV, the change in heat production as a function of the band gap resulted in the self-heating of a small band gap (E_g = 1.2 eV) device, 575 W/m^2, to be more than twice that of a large band gap (E_g = 2.2 eV) device, 253 W/m^2. Further, the steady-state operating temperature at the maximum power point was modeled and shown to significantly vary between 30 °C for a large (2.2 eV) band gap device and 44 °C for a small (1.2 eV) band gap device in the example outdoor conditions of 1000 W/m^2 irradiance, 20 °C ambient temperature, and ca. 1 m/s wind speed. The self-heating-induced temperature increment subsequently affected the power production predictions of different band gap devices, from −6 to −1%. The results presented here can improve the operation temperature and power production predictions of PSCs with alternative perovskite absorbers.

KEYWORDS: *perovskite solar cells, heat generation, cell temperature, temperature coefficient, power production estimation, energy yield modeling*

1. INTRODUCTION

Perovskite solar cells (PSCs) make up a fascinating group of emerging solar cells. Their power conversion efficiency has exceeded 25%[1,2] in less than 15 years since their first application in solar cells.[3] The high efficiency arises from the extraordinary material properties of perovskites, such as strong light absorption and long charge carrier diffusion length.[4] Furthermore, the material properties of perovskites are tunable by changing the composition. For example, a wide range of band gaps can be obtained.[5,6]

In this paper, the focus is on the effect of perovskite properties on the self-heating, temperature coefficient, and operation temperature of PSCs. The operation temperature is important for PSCs because it affects both their efficiency and stability. The effect of temperature on device operation originates not only from temperature-dependent material properties but also from the fact that temperature affects the charge carrier concentrations in semiconductors in general, that is, even without a direct dependence of material properties on the temperature. A higher temperature increases recombination and limits open-circuit voltage, which typically dominates the temperature coefficient of power production.[7,8] On the other hand, an elevated temperature[9−11] and temperature variations[12] present challenges for the device stability of PSCs. Although the thermal stability of PSCs is under active development,[13−16] a higher operation temperature is likely to accelerate material degradation, even in devices that are regarded very stable, such as silicon solar cells.[17] Thus, operation temperature matters, even if the critical issues of thermal stability[9,12] are solved.

Self-heating is used to describe the parasitic heat generation in the device during normal operation. When considering heat production in solar cells, it is good to remember the fundamental energy conservation: solar irradiation could be reflected away,

Received: January 11, 2024
Revised: April 23, 2024
Accepted: April 25, 2024

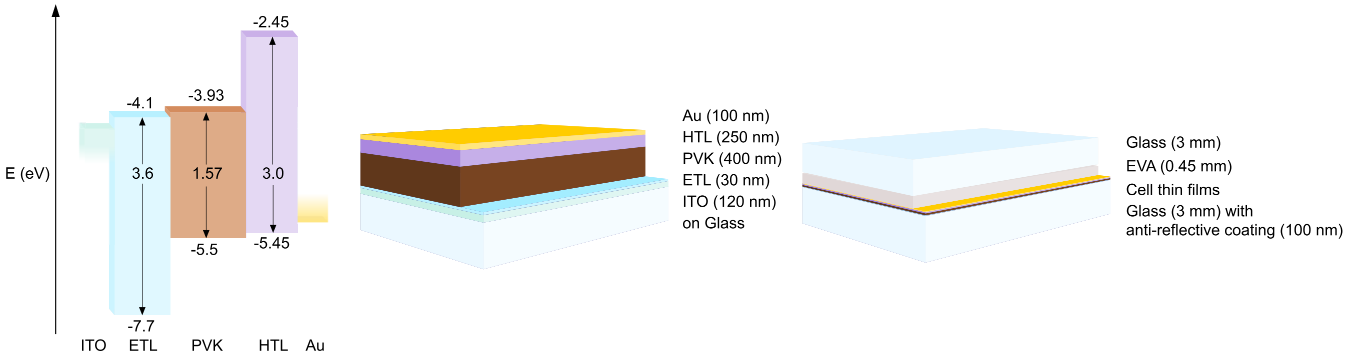

Figure 1. Initial energy levels and layer thicknesses of the simulated device. Ethylene vinyl acetate (EVA) encapsulation and back side glass were added into the device structure for the cell temperature calculation to consider realistic heat flux. Figures are not to scale.

transmitted, or absorbed, and the absorbed energy is then converted to either electricity or heat. Heat production in general and the detailed heating mechanisms are directly related to the operation and, especially, the loss mechanisms of solar cells. The heat production mechanisms in semiconductor solar cells[18−20] and specifically in PSCs[21] are described in the literature. They include parasitic absorption, thermalization, Joule heating, Peltier heating at electrodes (here called Peltier heat) and at heterojunction interfaces (here called heterojunction heat), and recombination heating. Parasitic absorption is absorption that occurs in a substrate or transport material, where it does not generate charge carriers and converts light to heat. Thermalization is the relaxation process of photogenerated electrons (holes) to the bottom (top) of the conduction (valence) band, and the excess energy of the absorbed photon becomes heat. Joule heat is the loss of electrical energy when a current is driven in a resistive material. Peltier heat describes the energy change when a current is driven over an energy level gradient at material interfaces. Recombination heating is the heat from nonradiative recombination. However, detailed heating mechanisms are seldom considered in PSC modeling.

In the current study, heat generation in planar PSCs is studied with coupled optoelectronic and coupled optical, electrical, and thermal (OET) simulations based on a one-dimensional transfer matrix and finite element methods. Specifically, the effects of the perovskite band gap, diffusion length (controlled by the bulk trap density), and layer thickness on the heat production and temperature coefficient of a planar PSC at a predefined cell temperature are simulated with the coupled optoelectronic model. Furthermore, the steady-state operation temperature and its effect on the power production in PSCs are investigated using the OET model to elucidate how the thermal differences induced by varied material properties are expected to affect the cell temperature and power production estimation under outdoor conditions. Detailed consideration of cell temperature is important because it could affect energy yield modeling over 10%.[22] The results can help estimate how changing the perovskite absorber affects the operation temperature and power production of a PSC.

The simulated device had a planar structure of glass/ITO/electron transport layer (ETL)/perovskite (PVK)/hole transport layer (HTL)/Au with different layer thicknesses and energy levels, as shown in Figure 1. The device models, including optical, electrical, and thermal operation and model couplings, are described in the Methods section. Applied optical, electrical, and thermal material properties are introduced in the Supporting Information (Table S2). The perovskite band gap and charge carrier mobility depend on cell temperature (Table S2), and band gap temperature dependence also affects the complex index of the refraction spectrum (which can be converted to the complex dielectric constant) in optical frequencies. The material properties of the ETL, PVK, and HTL were, respectively, based on those of SnO_2, $CH_3NH_3PbI_3$ (MAPI), and Spiro-OMeTAD. In later sections, material properties are varied to find their effect on the heat generation, temperature coefficient, and cell temperature.

2. RESULTS AND DISCUSSION

2.1. Device Operation at Different Cell Temperatures.

The current−voltage operation of the PSC in different predefined cell temperatures (T_{cell}s) was simulated to investigate the temperature dependence of device operation. An irradiance of 1000 W/m^2 with a standard AM1.5 spectrum was applied. Other ambient conditions and heat exchange of the device with the environment are considered in Section 2.3.

As is common for solar cells and previously reported for PSCs in computational[21] and experimental[23] studies, the open circuit voltage (V_{OC}) was found to decrease and the maximum power point (MPP) was found to shift to a smaller voltage as T_{cell} increased, as shown in Figure 2. The short circuit current density (J_{SC}) also slightly decreased.

The temperature coefficient of power production (β_{P}) provides a quantitative tool for comparing the temperature dependence of the power production in different devices.[8] Furthermore, β_{P} can be divided into its components

$$\beta_{\mathrm{P}} = \beta_{J_{\mathrm{SC}}} + \beta_{V_{\mathrm{OC}}} + \beta_{\mathrm{FF}} \tag{1}$$

if all current−voltage (*IV*) performance parameters depend linearly on the temperature,[8] which gives additional information on the origins of the dependence. Here, all *IV* parameters changed linearly enough under the temperature variation that the slopes of the linear fits described their temperature dependence (Figure S5). The temperature coefficients of power production, V_{OC}, and J_{SC} were negative, while that of the fill factor (FF) was slightly positive, as shown in Table 1. The open circuit voltage declined the most, and the effect on the short circuit current density and FF was 1 order of magnitude smaller. It is typical for V_{OC} to have the strongest temperature dependence because of higher temperature accelerating recombination.[7,8] Values of a similar order of magnitude for experimental β_{P}s for PSCs with different materials and configurations have been reported in the literature, varying from β_{P} = −0.08%/°C to β_{P} = −0.18%/°C.[23−26] The temperature coefficient of power production obtained here

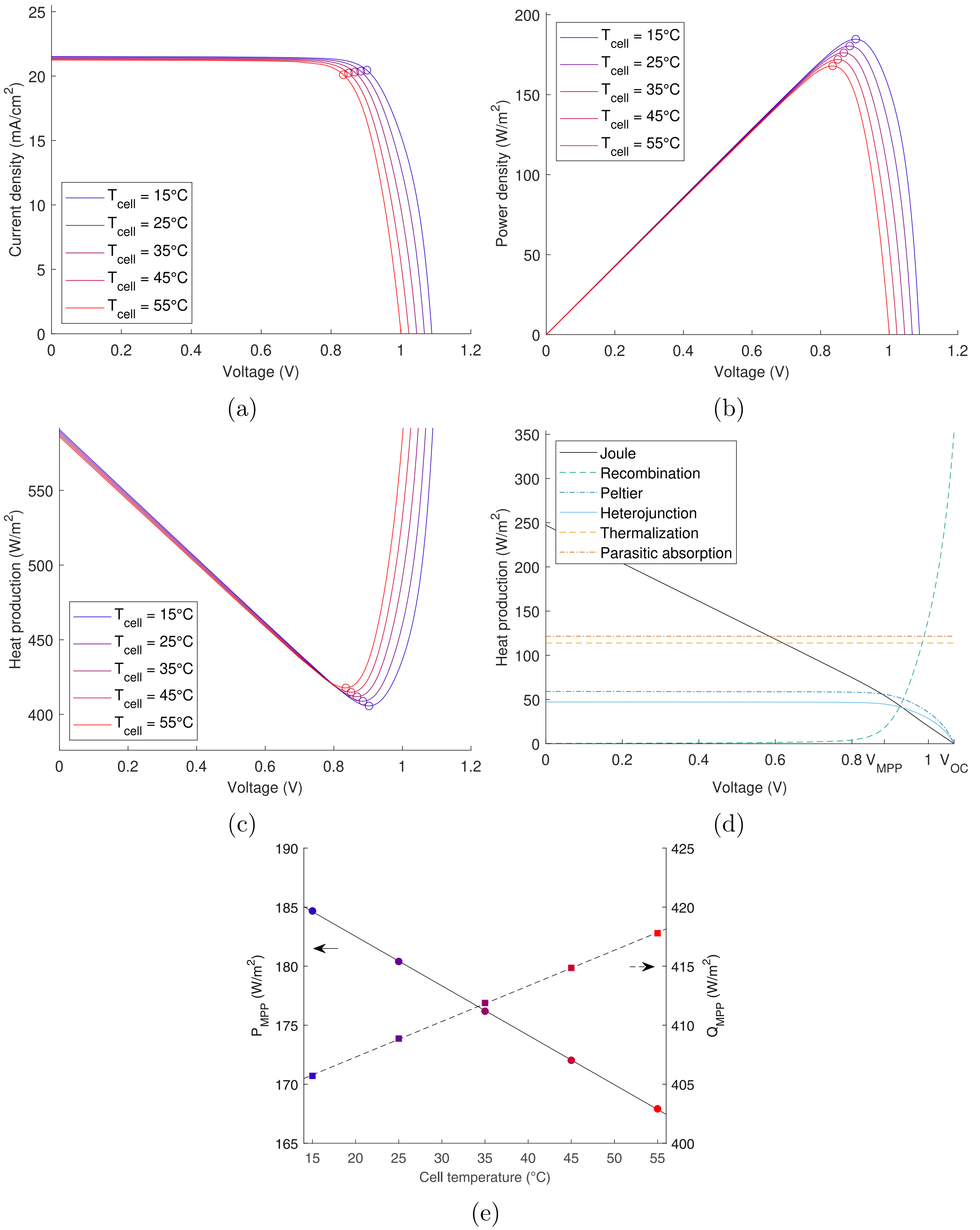

(a) (b) (c) (d) (e)

Figure 2. (a) Current density, (b) power production, and (c) heat production as a function of the voltage bias at different cell temperatures. (d) Voltage bias dependency of different heating mechanisms (obtained in 25 °C). (e) Power conversion to electricity and heat, respectively, at MPPs [marked with circles in (a)−(c)] with linear fits.

was slightly larger (more negative) at $\beta_P = -0.23\%/°C$ because of $\beta_{V_{OC}}$, which was somewhat larger than the values found in the literature.[23,25,26] Because the carrier concentration and recombination significantly affect $\beta_{V_{OC}}$ and β_P,[7] it is possible

Table 1. Temperature Coefficients of the *IV* Parameters

parameter	J_{SC}	V_{OC}	FF	η
β (%/K)	−0.03	−0.21	0.01	−0.23

that the obtained, slightly larger $\beta_{V_{OC}}$ than the experimental values was because of the applied value of the interface trap density (see Table S2), which was on the higher end of reported interface trap densities.[18] However, the obtained $\beta_{V_{OC}}$ was smaller than typical $\beta_{V_{OC}}$s of conventional semiconductor solar cells,[24,27] as is characteristic for PSCs.

One distinct feature of perovskites contributing to the small $\beta_{V_{OC}}$ is their property of the band gap increasing with the temperature, which is usually the opposite for most semiconductors.[8] Here, it was defined that $dE_g/dT = 0.25$ meV/K.[28] The temperature dependence of the band gap only had a minor effect on the power production temperature coefficient of the standard device because of opposing effects on different *IV* parameters, which effectively canceled each other out (Figure S6). However, a smaller absolute β_P could be obtained with a larger dE_g/dT value in the case of low band gap devices and with a smaller dE_g/dT in the case of large band gap devices (Figure S6).

Considering the heat generation in solar cells, it is important to note that the harvested energy is converted to either electrical power or heat. Thus, like power production, self-heating also depends on the voltage bias.[20,21] This power conversion balance in the cell is visible in Figure 2b,c: self-heating decreases as much as power production increases for each temperature when increasing the voltage bias toward the MPP and vice versa after the voltage exceeds the MPP. Increasing heat production around V_{OC} (Figure 2c) is because of strongly increasing recombination while Joule heating, Peltier heating, and heterojunction heating approach zero because they are proportional to the current, as shown in Figure 2d. Thermalization and parasitic absorption mainly depend on the optics, that is, absorption in the perovskite and other materials, respectively, and do not directly depend on the voltage bias (Figure 2d). However, temperature affects the band gap and optical constants of PVK, so the harvested energy also changes as a function of temperature, causing the reflection to slightly increase with the increasing temperature (Figure S7). The change in reflection explains why the sum of power and heat production slightly decreases with increasing temperature in Figure 2e, which shows how electric power production and heat generation depend on T_{cell}.

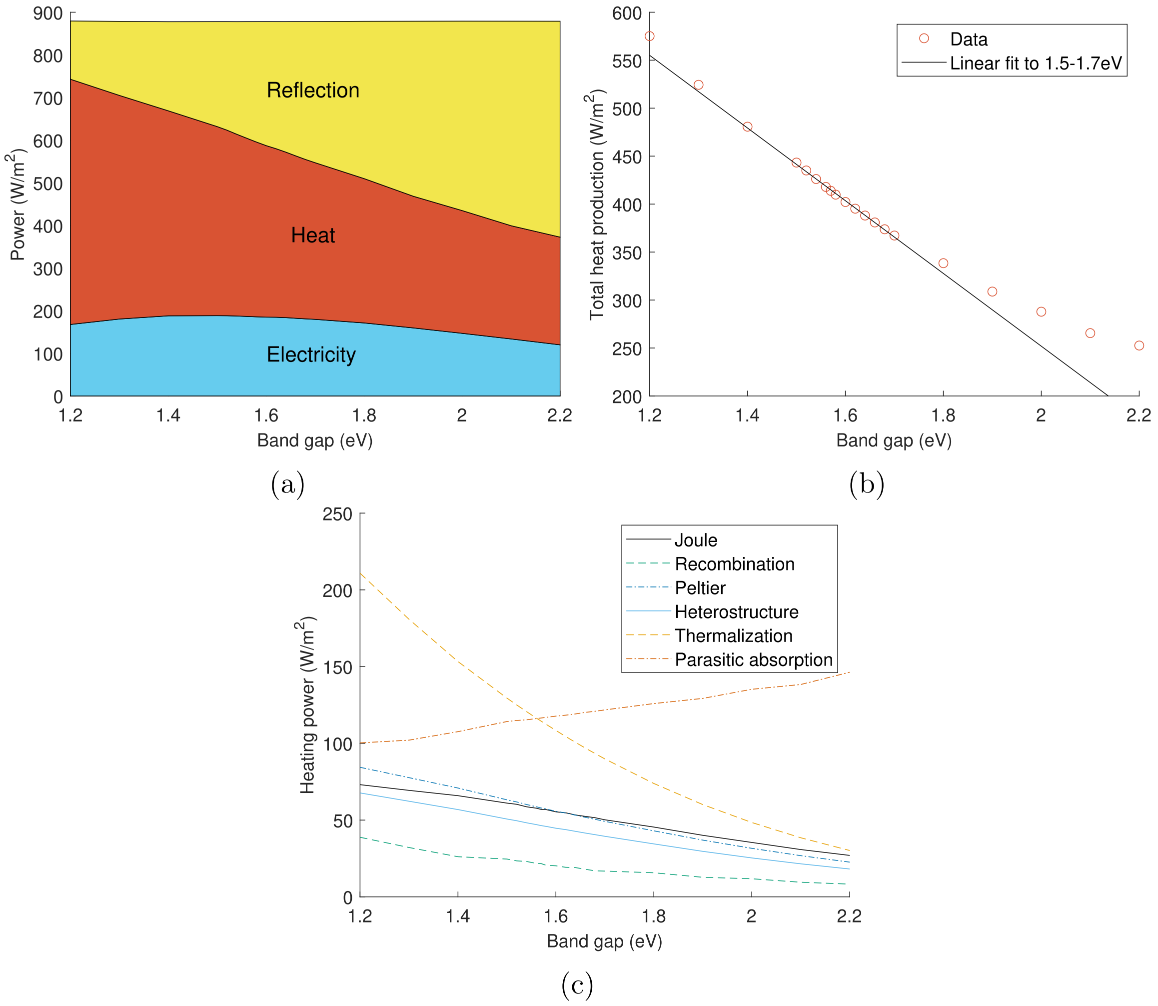

(a)

(b)

(c)

Figure 3. (a) Power conversion to electricity and heat and reflection of the PSC as a function of the band gap. The PVK layer thickness for each band gap was chosen separately to maximize the electric power production of the specific point. (b) Total heat production with a linear fit over the band gap range of 1.5−1.7 eV. (c) Heat source terms as functions of the band gap.

https://doi.org/10.1021/acsaem.4c00077

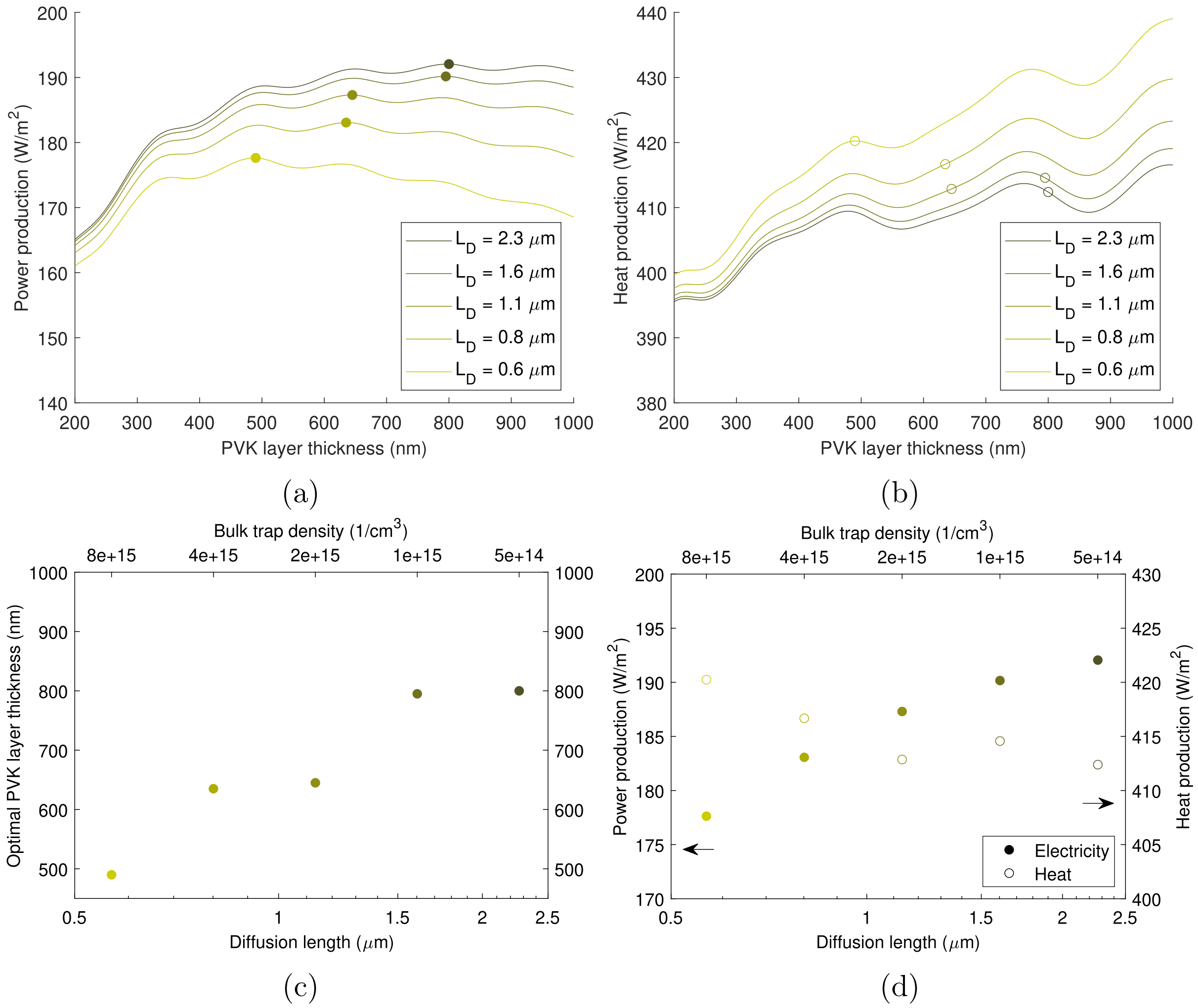

(a) (b) (c) (d)

Figure 4. (a) Power and (b) heat production as a function of the PVK layer thickness for different diffusion lengths. The points of maximum power production are highlighted with circles in (a,b). (c) Optimal PVK layer thickness as a function of diffusion length. (d) Power and heat productions, respectively, as functions of diffusion length when diffusion length-specific optimal PVK layer thicknesses were applied.

2.2. Effect of Active Material Properties on Device Operation.

The perovskite band gap was found to significantly affect heat production in the modeled device. The band gap varied over a wide range, 1.2−2.2 eV, while other material properties were maintained as constants apart from the HTL band gap, which was varied along the PVK band gap to maintain a constant valence band offset. A predefined $T_{\mathrm{cell}} = T_{\mathrm{stc}} = 25$ °C was applied to specify the first order effects of the band gap. The second order effects, including the change in T_{cell} and its repercussions on heat production itself, are discussed in Section 2.3.

Over the studied band gap range, electric power production reached a maximum at 1.52 eV, while heat production decreased and reflection increased monotonically, as shown in Figure 3a. The presented behavior of the electricity and heat productions and reflection (non-absorption) of different band gap devices agrees qualitatively with the reported theoretical efficiency limit calculations.[29,30]

The obtained power production maximum around 1.5 eV is larger than what is typically found in detailed balance calculations. The difference is because the recombination is dominated by nonradiative Shockley−Read−Hall recombination. A similar shift of the maximum to a larger band gap than the radiative limit optimal band gap with the increasing share of nonradiative recombination was already shown in the original paper by Shockley and Queisser.[31]

Heat generation of the $E_g = 1.2$ eV device, 575 W/m^2, was more than twice than that of the $E_g = 2.2$ eV device, 253 W/m^2, as shown in Figure 3a,b. The decrease in heating was faster at lower band gaps and slowed with the increasing band gap. A quasi-linear range of heat production in the most common band gap range of single junction PSCs, 1.5−1.7 eV, was observed, and a slope of −0.38 W/(m^2 meV) was obtained from the linear fit (Figure 3b). Three kinds of behaviors in the individual heat terms can be noted in Figure 3c: (1) parasitic absorption is the only term that increased with the band gap, (2) recombination, Joule, Peltier, and heterostructure heating decreased with the increasing band gap as photogeneration (G_{ph}) decreased, and (3) thermalization decreased with the decreasing G_{ph} and more energy was extracted per excited electron from the remaining G_{ph}, so its change was more pronounced than that of the other decreasing heat terms.

The total power was closely conserved at approximately 880 W/m^2 instead of 1000 W/m^2 as it should be because the wavelength range of 300−1300 nm that was applied in the calculations includes 88% of the total power of the standard AM1.5 spectrum. The wavelength range was restricted because of the availability of optical constant data for large wavelengths.

https://doi.org/10.1021/acsaem.4c00077
ACS Appl. Energy Mater. XXXX, XXX, XXX−XXX

Considering the low energy irradiance outside the applied range ($\lambda > 1300$ nm), most of the power should be reflected, as is the case for all below the band gap irradiance (Figure S8). However, some near-infrared irradiance is expected to be absorbed, for example, because of free electron absorption in the contact and transport layers, thus increasing the parasitic absorption and total heating.

In Figure 3, band gap-specific optimal PVK thicknesses were applied (Figure S10c). The variation of the optimal thickness was mainly because of variations in photogeneration, which originated from the (partial) coherence of light in thin layers (Figures S1 and S9). Local power production maxima shifted to smaller layer thicknesses with the increasing band gap, but the global optimum shifted back from a local maximum of a smaller layer thickness to another of a larger thickness as the band gap increased (Figure S10a). Overall, the effect of the band gap on the optimal layer thickness was minor compared with that of the diffusion length, as will be discussed later. The relative difference in power production between the band gap-specific optimal PVK thickness and a constant thickness of 700 nm was less than 1% with all the band gaps (Figure S10d). The material parameters applied here give a diffusion length of approximately 1.0 μm.

An increasing trend in heat generation as a function of the PVK layer thickness was noticed, but the effect was more moderate than the effect of the band gap, and the self-heating of large band gap devices even slightly decreased with the increasing PVK thickness (Figure S10). This growth was because of stronger recombination and increments in heating mechanisms that are proportional to the current, that is, Joule heat, Peltier heat, and heterojunction heat, which increased with higher photogeneration (Figure S11). The decrease for the large band gap devices was due to reduced parasitic absorption. A thicker PVK layer has been reported to increase the recombination and cell temperature at V_{OC},[32] but the effect on cell temperature was much more restrained in the current work.

The band gap was also found to affect the temperature coefficients of the cell. A larger band gap produced smaller $\beta_{V_{OC}}$ and β_P than a lower band gap, while the effect on $\beta_{J_{SC}}$ was mostly the opposite but much smaller (Figure S13). The FF temperature coefficient increased with the band gap and PVK thickness at first but saturated between −0.05 and 0%/K for a PVK thickness larger than 500 nm with all band gaps. Altogether, β_P mostly followed the changes in $\beta_{V_{OC}}$, and a larger band gap resulted in a smaller β_P, as suggested in the refs 7 and 8.

Although the band gap had little effect on the layer thickness dependence of PSCs, the diffusion length was found to notably affect the PVK thickness dependence, as shown in Figure 4. Here, the diffusion length was controlled by the bulk trap density according to eqs 2−4[33]

$$L_d = \sqrt{D\tau} \tag{2}$$

$$D = \mu \frac{k_B T}{q} \tag{3}$$

$$\tau = \frac{1}{N_t v_{th} \langle \sigma \rangle} \tag{4}$$

where L_d is the diffusion length, D is the diffusion constant, τ is the carrier lifetime, μ is the carrier mobility, k_B is the Boltzmann constant, T is the temperature, q is the elementary charge, N_t is the trap density, v_{th} is the thermal velocity of carriers, and $\langle \sigma \rangle$ is the average capture cross-section of carriers. The trap density was defined as a function of the position, and the effect of changing the bulk trap density on the diffusion length is presented in Figure S3. Mobility, thermal velocity, and average capture cross-section could also affect the diffusion length, but they were kept as constants for comparability.

As already observed with the different band gap devices, there was an increasing trend in electric power production with the increasing PVK layer thickness until reaching a maximum, after which the production decreased for all of the diffusion lengths, as shown in Figure 4a. The diffusion length, however, showed a more interconnected effect with the PVK thickness than the band gap. For shorter diffusion lengths, the maximum was reached with a smaller thickness, and the decrease in power production after the maximum was steeper than with longer diffusion lengths, as presented in the literature.[34,35] The logarithmic proportionality of the optimal PVK thickness to the diffusion length is shown in Figure 4c. The stepwise increase in the optimal thickness is because of the local maxima, which followed the oscillations in G_{ph}, as discussed earlier. Maximum power production also showed an increase that is proportional to the logarithm of the diffusion length, but the benefit of a longer L_D decreases because the improvements in absorption and G_{ph} become smaller and smaller with increasing layer thickness (Figure 4d).

For the heat production, the longer diffusion length resulted in reduced heating and also milder dependence on the PVK thickness (Figure 4b). An increasing trend in heat production for thicker PVK layers was noticed for all diffusion lengths, but stronger growth was obtained with shorter diffusion lengths. Of the specific heating terms, shorter diffusion length mainly increased Joule heating and recombination heating, which caused an accelerating heating rate with the increasing PVK thickness (Figure S12). Peltier and heterojunction heating even decreased with a shorter diffusion length, which may be because of a reduced current, but their changes were smaller than those of Joule and recombination heating (Figure S12). Reflection, parasitic absorption, and thermalization were constants under diffusion length variation (although not for different PVK thicknesses) because bulk trap density, and subsequently diffusion length, was considered independent of optical constants. Considering the total heat production in diffusion length-specific optimal PVK thicknesses, a decreasing trend was noticed with longer diffusion lengths despite the subsequently thicker optimal PVK layers, as shown in Figure 4d.

Diffusion length mainly affected β_P via β_{FF}, and the effect depended on the PVK thickness (Figure S14). There was no difference in β_{FF} between different L_Ds with 200−400 nm thick PVK layers, but with a thicker PVK layer, L_D made a small difference: $\beta_{FF} = 0.03\%/K$ ($L_D = 2.3\ \mu m$) and $\beta_{FF} = -0.02\%/K$ ($L_D = 0.6\ \mu m$) were obtained with a PVK thickness of 1000 nm. $\beta_{J_{SC}}$ and $\beta_{V_{OC}}$ maintained their respective values within roughly 0.02%/K with different diffusion lengths. Overall, the diffusion length affected the temperature coefficients far less than the band gap did.

The results in Figure 4 were calculated for a band gap of 1.57 eV. The effect of the diffusion length on different band gap devices was essentially analogous, but smaller band gap devices were affected somewhat more strongly than large band gap devices (Figure S15). The difference could be because of stronger absorption because both power and heat productions depend on the photogeneration.

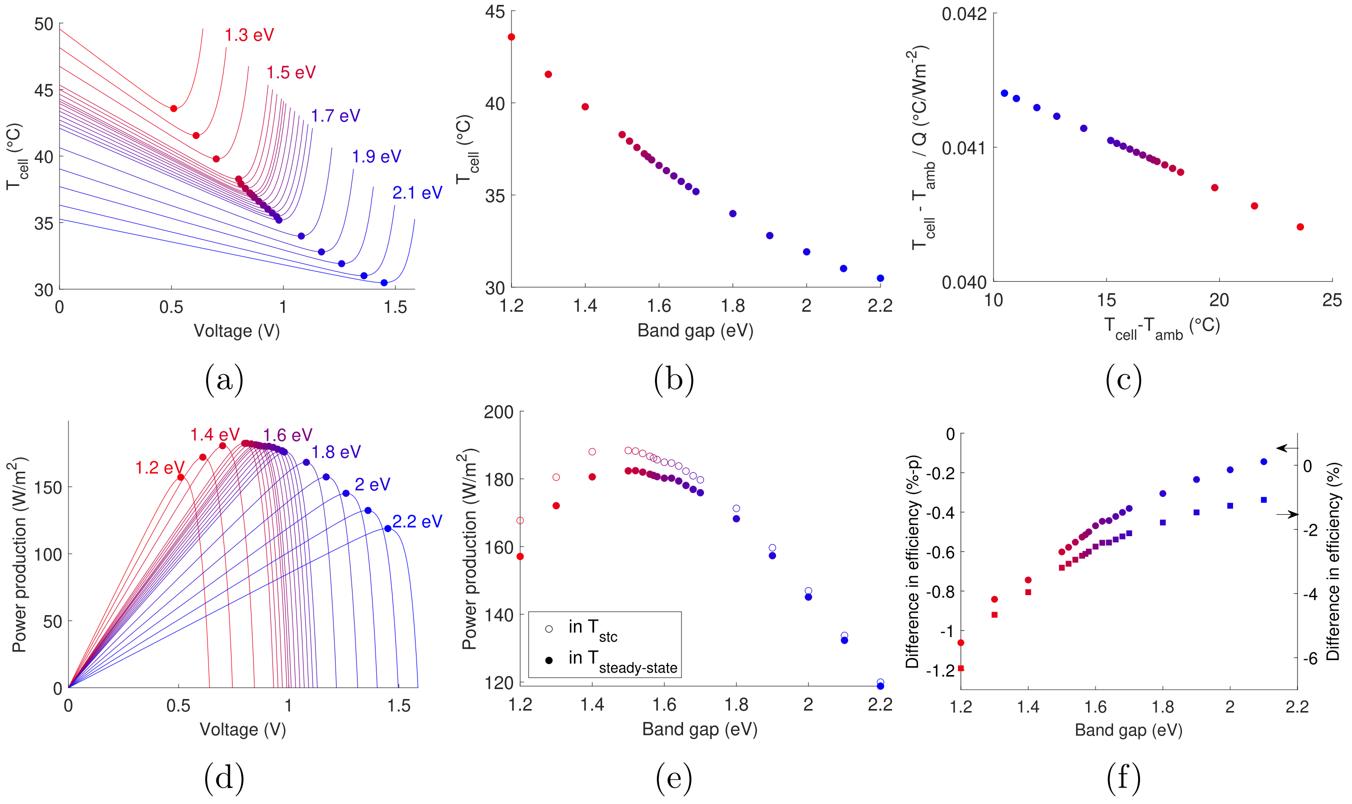

Figure 5. Steady-state operating temperature as a function (a) of voltage for different band gaps and (b) of the band gap in the respective MPPs [MPPs marked with circles in (a)]. (c) Temperature increment above the ambient temperature per heat production at the respective MPPs as a function of cell temperature above the ambient temperature. (d) Power production as a function of voltage for different band gap PSCs, each in specific steady-state temperature. (e) Respective maximum power production estimations at the STC (25 °C) and at simulated steady-state operation temperatures for different band gap PSCs. (f) Temperature-induced difference in efficiency estimates between the STC and steady-state temperatures as a function of the band gap.

2.3. Cell Temperature and Power Production Estimation of Different Band Gap Devices.

The coupled optoelectronic model at a predefined cell temperature was applied to show first how temperature affects the operation of planar PSCs and then how self-heating in these devices depends on the active material properties. In this section, the heat transfer model is coupled to the optical and electrical ones to simulate the effect of these two phenomena on the operation temperature and power production of PSCs in outdoor conditions. Exemplary weather conditions with the irradiance of 1000 W/m^2 with the standard AM1.5 spectrum and additionally the ambient temperature of T_{amb} = 20 °C and convection coefficients of 10 W/(m^2 K) and 5 W/(m^2 K) for the front and back side, respectively, corresponding to a wind speed of ca. 1 m/s[36] were applied.

Steady-state temperature followed the behavior of heat production under a voltage bias, as shown in Figure 5a. The temperature decreased until the MPP and then increased rapidly toward V_{OC}. The obtained steady-state operation temperatures at respective MPPs varied from 30 °C of the E_g = 2.2 eV device to 44 °C of the E_g = 1.2 eV device, as shown in Figure 5b. Here, the focus is on the effect of perovskite properties on the heat generated within the cell, but it is good to remember that the cell temperatures are subject to varying ambient conditions. Cell temperature is expected to depend almost linearly on both irradiance and ambient temperature, respectively, as has been reported for silicon solar cells.[37] A difference between the cell types would be expected in the linear dependence on the irradiance. Irradiance scales the heat production in the cell, but the slope is determined by the device properties because of their effect on heat production in the cell, as presented in Section 2.2. Ambient temperature affects the cooling and is expected to influence PSCs like silicon solar cells.

The difference between the minimum (at the MPP) and maximum (at 0 V or V_{OC}) temperatures reached the maximum of 7.1 °C with the same band gap as that for the maximum power production was obtained (1.52 eV), and similarly, the smallest difference of 4.8 °C was obtained with the smallest maximum power production (2.2 eV). The band gap-specific difference between temperature minima (at V_{MPP}) and maxima (at 0 V) resembled the band gap-specific power production in general (Figure S16). This is thought to follow from the facts that (1) the band gap determines the light harvesting efficiency and gives the maximum absorbed power, which equals the maximum heating, and (2) all the absorbed power is converted to either electricity or heat. The band gap-specific optimal PVK thicknesses were again applied here.

The second-order effects of the band gap-dependent self-heating in an elevated T_{cell} were observed to magnify the difference in heat production between the devices of different band gaps (Figure S17). However, the change was rather small under the applied ambient conditions. For example, the slope of the heat production as a function of the band gap, fitted in the quasi-linear range, steepened from −0.38 W/(m^2 meV) (Figure 3b) to −0.39 W/(m^2 meV) (Figure S17b). Thus, the most significant effect on heat production arose from the first-order effects of the band gap.

The "cost of self-heating", that is, how much 1 W/m^2 of heating increases the operation temperature above the ambient temperature, was found to be approximately 0.04 °C/Wm^{-2}. This value basically describes the cooling rate, which depends on the environmental conditions, especially wind speed, whereas irradiance affects heat generation. Because both the radiative and convective heat exchange rates increase with a larger temperature gradient, the value in general depends on the operation temperature so that it takes progressively more and more heat to increase the temperature by one degree, as shown in Figure 5c. However, the effect is very small, and the aforementioned factors affecting the cooling rate dominate in the practical range of PSC operation temperatures. The cooling rate can also be affected by device installation[38] and active or passive cooling technologies,[39] for example, advanced optical techniques[40,41] or heat sinks. The application of an additional cooling technology could decrease the cell temperature. However, many factors, such as panel size and technology as well as climate conditions, should be considered when evaluating and comparing different cooling technologies.[39]

The power production of all devices decreased when changing from the standard test conditions (STC) to outdoor conditions because of the higher operation temperature and negative temperature coefficient of power production, as shown in Figure 5e,f. Because low band gap devices experienced the strongest heating and highest operation temperature, their efficiency deviated the most from the STC prediction, up to −6% relative change. The relative difference was approximately −3%, with a band gap of around 1.6 eV, while the effect on large band gap devices was smaller at −1%. The difference originates from the temperature increment and temperature coefficient of power production, both of which were found to be smaller for large band gap devices.

Performance advantage of larger band gap materials in hot and humid climates has been reported in the literature.[42] The presented results fit into this picture, but detailed device optimization in specific locations and climates requires comprehensive consideration of irradiance, temperature, and other weather conditions, and this has been left for the future work.

Altogether, the cell temperature is a combined product of the heating and cooling. The focus in this article was on the heating because cooling and the effect of environmental conditions are more investigated topics, probably because they are the variables affecting T_{cell} once the cell has been manufactured and is up and running. It is indeed important to consider cooling and its dependence on different environmental conditions. Detailed consideration of cell temperature in specific environmental conditions and its effect on energy yield modeling has been highlighted in the literature.[22] Considering the defined environmental conditions here, the present results provide neither the minimum nor the maximum limit of the operating temperature of PSCs but give an estimation of the common operating conditions with an installation that also allows back-side cooling. However, perovskites offer a unique opportunity to modify the properties of the active material, and thus, it becomes important to predict all of the effects arising from the potential changes in the absorber. Most importantly, the presented results provide a tool for estimating such changes in the heat generation and subsequently the temperature of PSCs. Interestingly, there was a larger than a factor of 2 change in the self-heating over the whole range of the investigated band gaps (Figure 3a,b). Therefore, under different cooling conditions resulting in a higher cell temperature, the difference between T_{cell}s would be expected to increase from what was already a substantial difference, as presented in the current results.

3. CONCLUSIONS

In the present study, computational simulations were carried out to investigate how the band gap, diffusion length, and layer thickness of the absorber affected the self-heating and *IV* parameter temperature coefficients of a planar PSC. Self-heating decreased with a slope of −0.38 W/(m^2 meV) as the band gap was increased in the quasi-linear range from 1.2 eV to 1.7 eV, after which the slope slightly relaxed. Over the entire range of the studied band gaps, the total heat production monotonically declined from 575 W/m^2 (E_g = 1.2 eV) to 253 W/m^2 (E_g = 2.2 eV), and the effect of the band gap on the heat production was similar for all layer thicknesses. On the other hand, the effect of the varying diffusion length was not as significant and depended also on the PVK layer thickness. A larger band gap was also found to improve the temperature coefficient of power production, that is, decrease the absolute temperature dependence, while a longer diffusion length showed a clear but less significant improvement. The effects of the band gap and diffusion length on the temperature coefficient of power production were mainly seen via the temperature coefficients of the open circuit voltage and FF, respectively. Furthermore, it was shown how the difference in self-heating between different band gap devices propagated to their steady-state operation temperatures and power production predictions in the modeled example outdoor conditions. Over a 10 °C difference in the steady-state operation temperature between different band gap devices and over 5% relative differences in band gap-specific power productions between realistic conditions and STC were observed over the studied band gap range of 1.2−2.2 eV. Based on the results, it is suggested to consider the dependence of self-heating on active material properties in device temperature modeling and, further, its effect on operation temperature and outdoor power production predictions.

4. METHODS

4.1. Optics. A net-radiation method[43] based on transfer matrix formalism[44−46] was applied to solve the normalized optical electric field at material interfaces for each wavelength. The local optical electric field in each layer was then calculated as a sum of contributions from both adjacent interfaces propagating in different directions.[46,47] The normalized local optical electric field $[E'(x, \lambda)]$ gives the local absorbed power per unit volume and wavelength by

$$A_j(x, \lambda) = P_{\text{in}}(\lambda)\alpha_j(\lambda)n_j(\lambda)|E'(x, \lambda)|^2 \quad (5)$$

where $P_{\text{in}}(\lambda)$ is the solar irradiance, $\alpha_j(\lambda)$ is the absorption coefficient of layer j, $n_j(\lambda)$ is the real part of the refractive index of layer j, and all are functions of wavelength λ. Photogeneration as a function of the position was calculated from the absorption in the perovskite $[A_{\text{PVK}}(x, \lambda)]$ as

$$G_{\text{ph}}(x) = \int_0^{\lambda_g} \frac{A_{\text{PVK}}(x, \lambda)}{hc/\lambda} \mathrm{d}\lambda \quad (6)$$

where $\lambda_g = hc/E_g$ corresponds to the band gap E_g and h and c, respectively, are Planck's constant and the speed of light.

4.2. Charge Transport. Electrical operation of the PSC was modeled by drift−diffusion equations.[48] The Poisson equation was solved for electric potential V and free electron (n) and hole (p) densities

$$\frac{d^2V}{dx^2} = \frac{q}{\epsilon_r}(n - p + N_d - N_a) \tag{7}$$

where q is the elementary charge, ϵ_r is the relative permittivity, and N_d and N_a are, respectively, the donor and acceptor doping densities. Steady-state electron (J_n) and hole (J_p) currents were defined by photogeneration and recombination (R) rates, as stated by current continuity

$$-\frac{dJ_n}{dx} = \frac{dJ_p}{dx} = q(G_{ph}(x) - R(x)) \tag{8}$$

4.3. Heat. Device temperature (T) was solved from the steady-state heat equation[49]

$$-k(x)\frac{\partial^2 T(x)}{\partial x^2} = Q(x) \tag{9}$$

where k is the material-specific thermal conductivity and Q is the total heat generation. The total heat generation was calculated as the sum of individual heat source terms presented below. Boundary conditions were defined by convective

$$H_{conv} = h(T_b - T_{amb}) \tag{10}$$

and radiative

$$H_{rad} = \epsilon\sigma(T_b^4 - T_{amb}^4) \tag{11}$$

heat exchanges with the environment, where h is the convection coefficient, ϵ is the emissivity of the surface material, σ is the Stefan−Boltzmann constant, T_{amb} is the ambient temperature, and T_b is the device temperature at the (front or rear) boundary.

4.3.1. Heating Mechanisms. Parasitic absorption in layer j was defined as

$$Q_{ParAbs,j}(x) = \int_0^\infty A_j(x, \lambda)\, d\lambda \tag{12}$$

where A_j is the absorption in any layer and at any wavelength except PVK and $\lambda \in [0, \lambda_g]$. Thermalization:[20]

$$\begin{aligned} Q_{therm}(x) &= \int_0^{\lambda_g} A(x, \lambda)\left(1 - \frac{E_g + 3k_BT}{hc/\lambda}\right) d\lambda \\ &= \int_0^{\lambda_g} G_{ph}(x, \lambda)(hc/\lambda - (E_g + 3k_BT))\, d\lambda \end{aligned} \tag{13}$$

Joule heating:[19,20]

$$Q_J = \vec{J}\cdot\vec{E} \tag{14}$$

where $\vec{J}$ is the total current density and $\vec{E}$ is the electric field. Recombination heating:[19]

$$Q_R(x) = R(x) \quad (E_c - E_v + 3k_BT) \tag{15}$$

where E_c (E_v) is the energy level of the conduction (valence) band. Here, a position-dependent carrier lifetime based on trap density distribution was applied for recombination to include both bulk and surface recombination in one term. Peltier heating:[20]

$$Q_{P,n} = J\ (E_c + 1.5k_BT - E_{fn}) \tag{16}$$

$$Q_{P,p} = J\ (E_{fp} - E_v + 1.5k_BT) \tag{17}$$

where E_{fn} (E_{fp}) is the quasi Fermi level of electrons (holes) at the electrode. Heterostructure heating is a type of Peltier heating originating from driving a current over an energy level change at heterojunctions interfaces and is defined as[19,21]

$$Q_{H,n} = -\vec{J}_n\cdot\frac{d\chi}{dx} \tag{18}$$

$$Q_{H,p} = -\vec{J}_p\cdot\frac{d}{dx}(\chi + E_g) \tag{19}$$

where χ is the electron affinity of a material.

4.4. Numerical Computation. COMSOL Multiphysics was used to solve the drift−diffusion and heat equations. The optical model was implemented in Matlab. The calculation of temperature and temperature-dependent optical properties, including, for example, band gap and photogeneration, was iterated until less than a 0.1 K change in the perovskite temperature was reached. Other model coupling, for example, including the temperature-dependent electrical operation of the cell, was incorporated in the COMSOL model. Solution convergence analysis for different mesh sizes (spatial discretization) is shown in the Supporting Information.

4.5. Perovskite Optical Constants for Different Band Gaps and Temperatures. The optical constants n and k of different band gap perovskites have been modeled based on those of another perovskite by shifting the n and k spectra via calculating new wavelengths for data points of n and k[50,51]

$$\lambda_{new} = f(\Delta\lambda_g) \tag{20}$$

where $\Delta\lambda_g$ refers to the wavelength change of the band gap. Different functions f have been proposed,[50,51] and the idea was also extended to calculate n and k of perovskites at different temperatures.[51]

Here, the n and k spectra for different band gap perovskites were produced based on those of MAPI with the following shift function

$$\frac{hc}{\lambda_{new}} = E_{new} = E + \Delta E_g = \frac{hc}{\lambda} + \frac{hc}{\Delta\lambda_g} \tag{21}$$

given a band gap shift of ΔE_g defined by intentional band gap determination or arising from temperature change.

■ ASSOCIATED CONTENT

Supporting Information

The Supporting Information is available free of charge at https://pubs.acs.org/doi/10.1021/acsaem.4c00077.

Further details of the optical model, descriptions of the material properties and perovskite property variation, effect of the spatial discretization on the numerical solution, and additional figures (PDF)

■ AUTHOR INFORMATION

Corresponding Author

Aleksi Kamppinen − *Department of Mechanical and Materials Engineering, University of Turku, 20500 Turku, Finland;* orcid.org/0000-0001-8696-6292; Email: aleksi.kamppinen@utu.fi

Authors

Heikki Palonen − *Department of Mechanical and Materials Engineering, University of Turku, 20500 Turku, Finland*

Kati Miettunen − *Department of Mechanical and Materials Engineering, University of Turku, 20500 Turku, Finland;* orcid.org/0000-0002-6564-6262

Complete contact information is available at:
https://pubs.acs.org/10.1021/acsaem.4c00077

Notes

The authors declare no competing financial interest.

■ ACKNOWLEDGMENTS

A.K. thanks the Jenny and Antti Wihuri Foundation and University of Turku Graduate School (UTUGS) grants for doctoral research. K.M. thanks the Research Council of Finland (BioEST, 336577).

REFERENCES

(1) Green, M. A.; Dunlop, E. D.; Yoshita, M.; Kopidakis, N.; Bothe, K.; Siefer, G.; Hao, X. Solar cell efficiency tables (version 62). *Prog. Photovoltaics Res. Appl.* **2023**, *31*, 651−663.

(2) Zhao, Y.; Ma, F.; Qu, Z.; Yu, S.; Shen, T.; Deng, H.-X.; Chu, X.; Peng, X.; Yuan, Y.; Zhang, X.; You, J. Inactive (PbI2)2RbCl stabilizes perovskite films for efficient solar cells. *Science* **2022**, *377*, 531−534.

(3) Kojima, A.; Teshima, K.; Shirai, Y.; Miyasaka, T. Organometal Halide Perovskites as Visible-Light Sensitizers for Photovoltaic Cells. *J. Am. Chem. Soc.* **2009**, *131*, 6050−6051.

(4) Gao, P.; Grätzel, M.; Nazeeruddin, M. K. Organohalide lead perovskites for photovoltaic applications. *Energy Environ. Sci.* **2014**, *7*, 2448−2463.

(5) Stoumpos, C. C.; Malliakas, C. D.; Kanatzidis, M. G. Semiconducting Tin and Lead Iodide Perovskites with Organic Cations: Phase Transitions, High Mobilities, and Near-Infrared Photoluminescent Properties. *Inorg. Chem.* **2013**, *52*, 9019−9038.

(6) Noh, J. H.; Im, S. H.; Heo, J. H.; Mandal, T. N.; Seok, S. I. Chemical Management for Colorful, Efficient, and Stable Inorganic−Organic Hybrid Nanostructured Solar Cells. *Nano Lett.* **2013**, *13*, 1764−1769.

(7) Green, M. A. General temperature dependence of solar cell performance and implications for device modelling. *Prog. Photovoltaics Res. Appl.* **2003**, *11*, 333−340.

(8) Dupré, O.; Vaillon, R.; Green, M. Physics of the temperature coefficients of solar cells. *Sol. Energy Mater. Sol. Cells* **2015**, *140*, 92−100.

(9) Domanski, K.; Alharbi, E. A.; Hagfeldt, A.; Grätzel, M.; Tress, W. Systematic investigation of the impact of operation conditions on the degradation behaviour of perovskite solar cells. *Nat. Energy* **2018**, *3*, 61−67.

(10) Chen, B.; Song, J.; Dai, X.; Liu, Y.; Rudd, P. N.; Hong, X.; Huang, J. Synergistic Effect of Elevated Device Temperature and Excess Charge Carriers on the Rapid Light-Induced Degradation of Perovskite Solar Cells. *Adv. Mater.* **2019**, *31*, 1902413.

(11) Mesquita, I.; Andrade, L.; Mendes, A. Temperature Impact on Perovskite Solar Cells Under Operation. *ChemSusChem* **2019**, *12*, 2186−2194.

(12) Schwenzer, J. A.; Rakocevic, L.; Gehlhaar, R.; Abzieher, T.; Gharibzadeh, S.; Moghadamzadeh, S.; Quintilla, A.; Richards, B. S.; Lemmer, U.; Paetzold, U. W. Temperature Variation-Induced Performance Decline of Perovskite Solar Cells. *ACS Appl. Mater. Interfaces* **2018**, *10*, 16390−16399.

(13) Song, W.; Rakocevic, L.; Thiruvallur Eachambadi, R.; Qiu, W.; Bastos, J. P.; Gehlhaar, R.; Kuang, Y.; Hadipour, A.; Aernouts, T.; Poortmans, J. Improving the Morphology Stability of Spiro-OMeTAD Films for Enhanced Thermal Stability of Perovskite Solar Cells. *ACS Appl. Mater. Interfaces* **2021**, *13*, 44294−44301.

(14) He, Z.; Li, M.; Jia, H.; Yu, R.; Zhang, Y.; Wang, R.; Dong, Y.; Liu, X.; Xu, D.; Tan, Z. Managing Interfacial Charged Defects with Multiple Active Sited Macrocyclic Valinomycin for Efficient and Stable Inverted Perovskite Solar Cells. *Adv. Mater.* **2023**, *35*, 2304918.

(15) Lintangpradipto, M. N.; Zhu, H.; Shao, B.; Mir, W. J.; Gutiérrez-Arzaluz, L.; Turedi, B.; Abulikemu, M.; Mohammed, O. F.; Bakr, O. M. Single-Crystal Methylammonium-Free Perovskite Solar Cells with Efficiencies Exceeding 24% and High Thermal Stability. *ACS Energy Lett.* **2023**, *8*, 4915−4922.

(16) Chen, H.; Yang, J.; Cao, Q.; Wang, T.; Pu, X.; He, X.; Chen, X.; Li, X. π-Interactions suppression of buried interface defects for efficient and stable inverted perovskite solar cells. *Nano Energy* **2023**, *117*, 108883.

(17) Chen, D.; Vaqueiro Contreras, M.; Ciesla, A.; Hamer, P.; Hallam, B.; Abbott, M.; Chan, C. Progress in the understanding of light- and elevated temperature-induced degradation in silicon solar cells: A review. *Prog. Photovoltaics Res. Appl.* **2021**, *29*, 1180−1201.

(18) Wachutka, G. Rigorous thermodynamic treatment of heat generation and conduction in semiconductor device modeling. *IEEE Trans. Comput. Aided Des. Integr. Circuits Syst.* **1990**, *9*, 1141−1149.

(19) Lindefelt, U. Heat generation in semiconductor devices. *J. Appl. Phys.* **1994**, *75*, 942−957.

(20) Shang, A.; Li, X. Photovoltaic Devices: Opto-Electro-Thermal Physics and Modeling. *Adv. Mater.* **2017**, *29*, 1603492.

(21) An, Y.; Wang, C.; Cao, G.; Li, X. Heterojunction Perovskite Solar Cells: Opto-Electro-Thermal Physics, Modeling, and Experiment. *ACS Nano* **2020**, *14*, 5017−5026.

(22) Lopez-Varo, P.; Amara, M.; Cacovich, S.; Julien, A.; Yaïche, A.; Jouhari, M.; Rousset, J.; Schulz, P.; Guillemoles, J.-F.; Puel, J.-B. Dynamic temperature effects in perovskite solar cells and energy yield. *Sustainable Energy Fuels* **2021**, *5*, 5523−5534.

(23) Jošt, M.; Lipovšek, B.; Glažar, B.; Al-Ashouri, A.; Brecl, K.; Matič, G.; Magomedov, A.; Getautis, V.; Topič, M.; Albrecht, S. Perovskite Solar Cells go Outdoors: Field Testing and Temperature Effects on Energy Yield. *Adv. Energy Mater.* **2020**, *10*, 2000454.

(24) Fu, F.; Feurer, T.; Weiss, T. P.; Pisoni, S.; Avancini, E.; Andres, C.; Buecheler, S.; Tiwari, A. N. High-efficiency inverted semi-transparent planar perovskite solar cells in substrate configuration. *Nat. Energy* **2016**, *2*, 16190.

(25) Deng, Y.; Van Brackle, C. H.; Dai, X.; Zhao, J.; Chen, B.; Huang, J. Tailoring solvent coordination for high-speed, room-temperature blading of perovskite photovoltaic films. *Sci. Adv.* **2019**, *5*, No. eaax7537.

(26) Moot, T.; Patel, J. B.; McAndrews, G.; Wolf, E. J.; Morales, D.; Gould, I. E.; Rosales, B. A.; Boyd, C. C.; Wheeler, L. M.; Parilla, P. A.; Johnston, S. W.; Schelhas, L. T.; McGehee, M. D.; Luther, J. M. Temperature Coefficients of Perovskite Photovoltaics for Energy Yield Calculations. *ACS Energy Lett.* **2021**, *6*, 2038−2047.

(27) Haschke, J.; Seif, J. P.; Riesen, Y.; Tomasi, A.; Cattin, J.; Tous, L.; Choulat, P.; Aleman, M.; Cornagliotti, E.; Uruena, A.; et al. The impact of silicon solar cell architecture and cell interconnection on energy yield in hot & sunny climates. *Energy Environ. Sci.* **2017**, *10*, 1196−1206.

(28) Singh, S.; Li, C.; Panzer, F.; Narasimhan, K. L.; Graeser, A.; Gujar, T. P.; Köhler, A.; Thelakkat, M.; Huettner, S.; Kabra, D. Effect of Thermal and Structural Disorder on the Electronic Structure of Hybrid Perovskite Semiconductor CH3NH3PbI3. *J. Phys. Chem. Lett.* **2016**, *7*, 3014−3021.

(29) Hirst, L. C.; Ekins-Daukes, N. J. Fundamental losses in solar cells. *Prog. Photovoltaics Res. Appl.* **2011**, *19*, 286−293.

(30) An, Y.; Ma, T.; Li, X. Energy Tracing of Photovoltaic Cells. *Sol. RRL* **2021**, *5*, 2100199.

(31) Shockley, W.; Queisser, H. J. Detailed balance limit of efficiency of p−n junction solar cells. *J. Appl. Phys.* **1961**, *32*, 510−519.

(32) Mehdizadeh-Rad, H.; Singh, J. Simulation of perovskite solar cell temperature under reverse and forward bias conditions. *J. Appl. Phys.* **2019**, *126*, 153102.

(33) Sze, S. M. *Physics of Semiconductor Devices*, 2nd ed.; Wiley: New York, 1981.

(34) Minemoto, T.; Murata, M. Device modeling of perovskite solar cells based on structural similarity with thin film inorganic semiconductor solar cells. *J. Appl. Phys.* **2014**, *116*, 054505.

(35) Malyukov, S.; Sayenko, A.; Ivanova, A. Numerical modeling of perovskite solar cells with a planar structure. *IOP Conf. Ser.: Mater. Sci. Eng.* **2016**, *151*, 012033.

(36) Notton, G.; Cristofari, C.; Mattei, M.; Poggi, P. Modelling of a double-glass photovoltaic module using finite differences. *Appl. Therm. Eng.* **2005**, *25*, 2854−2877.

(37) Usama Siddiqui, M.; Arif, A.; Kelley, L.; Dubowsky, S. Three-dimensional thermal modeling of a photovoltaic module under varying conditions. *Sol. Energy* **2012**, *86*, 2620−2631.

(38) Kurnik, J.; Jankovec, M.; Brecl, K.; Topic, M. Outdoor testing of PV module temperature and performance under different mounting and operational conditions. *Sol. Energy Mater. Sol. Cells* **2011**, *95*, 373−376.

(39) Koohestani, S. S.; Nižetić, S.; Santamouris, M. Comparative review and evaluation of state-of-the-art photovoltaic cooling technologies. *J. Cleaner Prod.* **2023**, *406*, 136953.

(40) Xie, W.; Xiao, C.; Sun, Y.; Fan, Y.; Zhao, B.; Zhang, D.; Fan, T.; Zhou, H. Flexible Photonic Radiative Cooling Films: Fundamentals, Fabrication and Applications. *Adv. Funct. Mater.* **2023**, *33*, 2305734.

(41) Ma, T.; An, Y.; Yang, Z.; Ai, Z.; Zhang, Y.; Wang, C.; Li, X. Thermodynamic Processes of Perovskite Photovoltaic Devices: Mechanisms, Simulation, and Manipulation. *Adv. Funct. Mater.* **2023**, *33*, 2212596.

(42) Peters, I. M.; Liu, H.; Reindl, T.; Buonassisi, T. Global Prediction of Photovoltaic Field Performance Differences Using Open-Source Satellite Data. *Joule* **2018**, *2*, 307−322.

(43) Santbergen, R.; Smets, A. H.; Zeman, M. Optical model for multilayer structures with coherent, partly coherent and incoherent layers. *Opt. Express* **2013**, *21*, A262−A267.

(44) Born, M.; Wolf, E. *Principles of Optics*, 4th ed.; Pergamon: Oxford, 1970.

(45) Katsidis, C. C.; Siapkas, D. I. General transfer-matrix method for optical multilayer systems with coherent, partially coherent, and incoherent interference. *Appl. Opt.* **2002**, *41*, 3978−3987.

(46) Pettersson, L. A. A.; Roman, L. S.; Inganäs, O. Modeling photocurrent action spectra of photovoltaic devices based on organic thin films. *J. Appl. Phys.* **1999**, *86*, 487−496.

(47) Burkhard, G. F.; Hoke, E. T.; McGehee, M. D. Accounting for Interference, Scattering, and Electrode Absorption to Make Accurate Internal Quantum Efficiency Measurements in Organic and Other Thin Solar Cells. *Adv. Mater.* **2010**, *22*, 3293−3297.

(48) Gray, J. L. *Handbook of Photovoltaic Science and Engineering*. Chapter 3; John Wiley & Sons, Ltd, 2003; pp 61−112.

(49) Blundell, S. J.; Blundell, K. M. *Concepts in Thermal Physics*, 2nd ed.; Oxford University Press, 2010.

(50) Manzoor, S.; Häusele, J.; Bush, K. A.; Palmstrom, A. F.; Carpenter, J.; Yu, Z. J.; Bent, S. F.; Mcgehee, M. D.; Holman, Z. C. Optical modeling of wide-bandgap perovskite and perovskite/silicon tandem solar cells using complex refractive indices for arbitrary-bandgap perovskite absorbers. *Opt. Express* **2018**, *26*, 27441−27460.

(51) Raja, W.; Allen, T. G.; Said, A. A.; Alharbi, O.; Aydin, E.; De Bastiani, M.; De Wolf, S. Temperature-Dependent Optical Modeling of Perovskite Solar Cells. *J. Phys. Chem. C* **2022**, *126*, 14366−14374.